The Mosaic of Surface Charge in Contact Electrification — **Source link** ↗

Hasan Tarik Baytekin, Alexander Z. Patashinski, Michal Branicki, Bilge Baytekin ...+2 more authors

Institutions: Northwestern University

Related papers:

- Electrostatic Charging Due to Separation of Ions at Interfaces: Contact Electrification of Ionic Electrets

- Flexible triboelectric generator

- Contact electrification of insulating materials

- A semi-quantitative tribo-electric series for polymeric materials: the influence of chemical structure and properties

- Theoretical study of contact-mode triboelectric nanogenerators as an effective power source

Edinburgh Research Explorer

The mosaic of surface charge in contact electrification

The mosaic of surface charge in contact electrification.

H. T. Baytekin, A. I. Patashinski, M. Branicki, B. Baytekin, S. Soh, B. A. Grzybowski*

Department of Chemistry and

Department of Chemical and Biological Engineering,

Northwestern University

2145 Sheridan Rd, Illinois 60208, USA.

* Correspondence to grzybor@northwestern.edu

ABSTRACT: When dielectric materials are brought into contact and then separated,
they develop static electricity. For centuries, it has been assumed that such
contact charging derives from the spatially homogeneous material properties (along the
material's surface), and that within a given pair of materials, one charges uniformly
positively and the other, negatively. We demonstrate that this picture of contact charging is
incorrect. While each contact-electrified piece develops a net charge of either positive or
negative polarity, each surface supports a random "mosaic" of oppositely charged regions
of nanoscopic dimensions. These mosaics of surface charge have the same topological
characteristics for different types of electrified dielectrics, and accommodate significantly
more charge per unit area than previously thought.

Contact electrification (*1-3*), which is the transfer of charge between two surfaces that are brought into contact and then separated, is one of the oldest areas of scientific study dating back to Thales of Miletus and his experiments with amber charging against wool (*4*). Although contact electrification has been successfully applied in several useful technologies (e.g., photocopying (*5*), laser printing (*6*), and electrostatic separations(*7*)) and chemical systems (*8,9*), remarkably little is known about the mechanism underlying this phenomenon, especially in non-elemental insulators (*1,10-15*). In this context, it is commonly assumed that (i) contact-charging derives from spatially homogeneous (on length-scales larger than molecular) surface properties of contacting materials *(1-3, 16-20)* and (ii) within a given pair of materials, one charges uniformly positively and the other, uniformly negatively (*1,7,15,21-24*) (Fig. 1A-upper right). These assumptions, however, make it difficult to explain numerous experimental observations whereby different particles made of the same bulk material (*25*) or even different macroscopic regions of the same sample (contact-charged (*26,27*) or probed using tips under bias (*28, 29*)) can exhibit different charging characteristics. Here, we show that contact-electrified non-elemental insulators are in reality random "mosaics" of positively (+) and negatively (-) charged regions of nanoscopic dimensions (Fig. 1A-lower right). These mosaics are universal in the sense as they comprise at least two characteristic length scales which are the same for different materials. The mosaics accommodate significantly more charge per unit area than previously estimated for contact electrification, but the overall/"net" charge on an electrified surface remains relatively small due to the "compensation" between the (+) and the (-) regions. In addition, the appearance of charge mosaics is accompanied by the changes in surface composition and by the transfer of material between the contacting

surfaces. Overall, our results indicate that contact electrification cannot be attributed to and predicted by the material's homogeneous properties alone, as is often assumed when constructing the so-called triboelectric series (*13, 30, 31*). Instead, control of contact charging phenomena requires the control of the chemical and possibly micromechanical properties at and near the surfaces of the contacting polymers.

The starting point of the present study is a recent observation that CE can occur between flat pieces of identical materials (*32*). According to the conventional view of contact electrification, this should not happen since the chemical potentials of the two surfaces/materials are identical and there is apparently no thermodynamic force to drive charge transfer. This scenario, however, assumes that CE is determined by the average compositions and properties of the materials (reflected in the chemical potentials) and completely neglects fluctuations from these averages. Indeed, a theoretical model accounting for these fluctuations can explain charging between identical materials assuming that each contacting surface is represented as a random "mosaic" of charge-donating (D) and charge-accepting (A) regions and charge transfer occurs in places where D and A overlap during contact (see Fig. 1A-lower right and, for further details, Ref. (*32*)).

While interesting in concept, the existence of charge mosaics has not been proven experimentally, even for the case of identical materials. Furthermore, it remains to be determined whether the mosaic picture is generalizable to contact-electrification between different insulators and, if so, on what scales the mosaics form. If the "mosaic" model were correct, then any contact-electrified surface should present itself as a union of (+) and (-) regions.

3

To test this hypothesis, we used the Kelvin Force Microscopy (KFM) to image surface potentials, Π, over various types of contact-electrified surfaces (e.g., polydimethylsiloxane, PDMS; polycarbonate, PC; polytetrafluoroethylene, PTFE; silicon; aluminum; see Supporting Online Material, SOM, Section 1). Concurrently, the overall/net charge on all the materials before and after electrification was measured using a Faraday cage connected to a high-precision electrometer (Keithley, 6517B). In all experiments, we verified that the results did not depend on (i) the time of contact (for times from 2 sec to 1.5 hrs), (ii) the pressure applied during contact (0.01 – 4.5 MPa) or (iii) the way in which the surfaces were separated (e.g., rapidly or slowly peeled off one another). We note that experiments using PDMS, in particular, rule out the possibility that uneven, "mosaic" charging would reflect imperfect contact between the surfaces (since PDMS is known to come into conformal contact with other polymers (*33*).

Figures 1B-D shows typical KFM maps. In all cases, the surfaces were not charged before CE ($\Pi \sim 0$; Fig. 1B). After contacting against other materials, however, the potential maps comprised a mosaic of (+) and (-) regions. Such maps were observed for all contacting materials (Figs. 1C and 1D), irrespective of whether the net charge was positive or negative, indicating that the mosaic charging is a generic feature of contact-electrified dielectrics. . As might be expected, the charges on the electrified pieces decayed with time after contact electrification. Figure 2A illustrates that the decay of the net charge follows, to a good approximation, first-order kinetics with the decay rate constants on the order of k_{dis}^{net} $\sim 10^{-3}$ s^{-1} similar to those recorded by others (*34*). This macroscopic decay originates from the discharging of the mosaics' individual patches (Fig. 2B). Analysis of potential scans

4

such as those shown in Fig. 2C indicates that discharging is first-order in time with rate constants on the order of $k_{dis}^{patch} \sim 10^{-3}$ s^{-1} (i.e., of magnitude similar to k_{dis}^{net}). Interestingly, the scans also reveal that charge does not migrate laterally within the electrified materials, such that the patches do no "blur" (see SOM, Section 2) and the geometric structure of the mosaics is preserved during their discharge. In the absence of lateral charge mobility, discharge is likely due to the collisions of the polymer surface with the molecules/ions/particles contained in the surrounding air. The previously observed rates of discharge via this so-called "external decay" are similar to those we estimated (34, 35).

Having established their presence, we investigated the geometric structure of the charge mosaics. To this end, we digitized the KFM potential maps into (+) and (-) regions (Fig. 3A) and characterized the boundaries separating +/- regions by the profiles of the so-called local box counting (LBC) dimension. This dimension is defined as $L_{BC}(\varepsilon) = -\dfrac{d \ln N(\varepsilon)}{d \ln \varepsilon}$, where $N(\varepsilon)$ is the minimum number of squares of size ε needed to cover the boundary curve (Fig. 3B). It is well known that the profiles $L_{BC}(\varepsilon)$ can provide more insight into the geometric differences and similarities at various scales than the asymptotic definition of the BC dimension, $D_{BC}(\varepsilon) = -\lim_{\varepsilon \circledR 0} \dfrac{\ln N(\varepsilon)}{\ln \varepsilon}$, familiar from fractal geometry *(36)*. Importantly, the analyses based on the LBC dimension lead to two major conclusions: (1) The $L_{BC}(\varepsilon)$ profiles are similar for different materials studied and at different length scales of analysis (Fig. 3C) and (2) the mosaic patterns can be described as random scalar fields involving at least two spatial length scales. To verify the second conclusion, we generated various types

of multi-scale, random fields and compared their structure (i.e., $L_{BC}(\varepsilon)$) with that of the experimental potentials obtained from the KFM scans. The random fields were generated by distributing white-noise fluctuations over a collection of independent meshes of different characteristic mesh-sizes σ (see SOM, Section 3 for more details). None of the patterns involving only one fluctuation length scale (Fig. 3D) matched the $L_{BC}(\varepsilon)$ profiles observed in experiments. On the other hand, good agreement was achieved using a random field comprising two fluctuation length scales (Fig. 3E). The best agreement corresponded to length scales $\sigma_1 = 0.45\ \lceil m$ and $\sigma_2 = 0.044\ \lceil m$ (red dotted line in Fig. 3C) – these length scales were similar for various types of electrified surfaces.

The σ_1 length scale of several hundreds of nanometers is clearly discernible in the potential maps in Figure 1. The smaller, σ_2-scale regions within the larger patches can be resolved under high-resolution KFM (Fig. 4A), and the magnitudes of charges distributed over these regions can be estimated from the potential profiles. This is illustrated in Fig. 4B which shows a typical potential line-scan over two nearby regions of opposite polarities. Importantly, this experimental potential (and other scans similar to it) fits well to the potential calculated for a "dipole" of two oppositely charged surface "patches," each containing ca. 500 elementary charges of the same polarity. Given that the size of the patches is in tens of nm, one can deduce the surface charge density of approximately one elementary charge per ~10 nm^2, or on the order of $\lceil C/cm^2$. We note that this value is significantly higher than the "net" surface charge densities measured by Faraday cup for macroscopic electrified polymers – typically, these values are in nC/cm^2 range (*32,37*). We surmise, however, that there is no inconsistency here: While the small, individual islands

within the "mosaic" are highly charged, the total areas of all the "+" and "-" regions are similar (typically, within ~0.1% as determined from images like those in Fig. 3A), and so the charge "compensation" results in a relatively small net charge over larger areas. An important corollary is that in CE, more charges are being transferred than had previously been assumed based on the macroscopic charge densities – in other words, CE is not a "sparse" event affecting ca. one in ~ 10,000 surface groups, but a more probable event affecting ca. one in ~100 groups on the material's surface.

Of course, the above observations do not explain how and why the charge mosaics emerge. To gain at least some insights into the nature of this process, we performed a series of experiments using Confocal Raman Spectroscopy (CRS) and also X-ray Photoelectron Spectroscopy (XPS). The Raman spectra were recorded with spatial resolution down to 250 nm (i.e., commensurate with the σ_1 scale of the charge mosaics) and are summarized in Fig. 5A and 5B. The two relevant observations we make is that contact electrification is accompanied by the changes in material's composition near the surface (Fig. 5B; for the Raman spectra at different depth, see SOM, Section 4) and also by increased surface "patchiness" (Fig. 5A) resembling that of charged mosaics. In terms of composition, contact electrification gives rise to the increase in the intensity of signals that can be assigned ([38-40]) as oxidized species (e.g., for PDMS, $SiCH_2COOH$ with C=O band stretches at 1642 cm^{-1} and 1710-1730 cm^{-1}, as well as carboxy or peroxy acids with C=O bands between 1730-1830 cm^{-1}). Interestingly, in previous works on the degradation of elastomers (such as PDMS used here) ([39]), it has been demonstrated that these oxidized species form as a result of homolytic and heterolytic bond-breaking and subsequent reaction with atmospheric oxygen and/or water. In the context of our present studies, these

findings suggest that contact charging might involve heterolytic bond breaking and, if so, the emergence of the charge mosaics could be related to the transfer of charged material "patches" between the contacting materials. This hypothesis of material transfer during contact electrification of dielectrics has been considered for a long time (*41,42*) albeit has not been universally accepted. Our XPS studies on pairs of polymers that feature distinct elemental peaks confirm the presence of material transfer. One especially convenient pair to study is PDMS (containing Si but not F) and PTFE (containing F but not Si). The spectra in Figures 5C and 5D show that upon contact, the F 1s signal at 690 eV appears in the spectrum of PDMS, while distinct Si 2p at 102.5 eV and O 1s at 533 eV peaks appear in the spectrum of PTFE (the intensities of these peaks also increase with the number of polymer-polymer contacts). These and other measurements (see SOM, Section 5 for the XPS of PDMS/PC and PDMS/PMMA pairs) indicate that contact electrification is, indeed, accompanied by material transfer.

A picture that then emerges is that contact-electrification is a complex process involving a combination of, at least, bond cleavage, chemical changes, and material transfer occurring within distinct patches of nanoscopic dimensions. The exact relationship between these effects – and possibly also those due to the presence of surface water (*15*) and local electric fields (*43*) – remains unclear but prompts several intriguing questions for future research (e.g., How is charge polarity related to the types of bonds broken in given regions? Does the mechanics of material transfer determine the length-scale of the mosaics?). Understanding these and other effects will require implementation of experimental techniques that could probe the changes in local material properties of the dielectrics with molecular–scale resolution. Finally, in light of our findings, it becomes clear why previous

attempts to construct the so-called triboelectric series based on the "average" material properties (*30,31*) often gave ambiguous results – in reality, it is the nanostructure of the material's surface and the fluctuations in this structure that determine the macroscopically observed charging trends.

References and Notes:

1. J. Lowell, A.C. Rose-Innes, Contact electrification. *Adv. Phys*. **29**, 947-1023 (1980).

2. R. G. Horn, D. T. Smith, Contact electrification and adhesion between dissimilar materials. *Science* **256**, 362-364 (1992).

3. R. G. Horn, D. T. Smith, A. Grabbe, Contact electrification induced by monolayer modification of a surface and relation to acid–base interactions. *Nature* **366**, 442-443 (1993).

4. P. F. O'Grady, *Thales of Miletus: The Beginnings of Western Science and Philosophy* (Ashgate, Aldershot, 2002).

5. L. B. Schein, *Electrophotography and Development Physics* (Laplacian, Morgan Hill, CA, 1996).

6. D. M. Pai, B. E. Springett, Physics of electrophotography. *Rev. Mod. Phys.* **65**, 163-211 (1993).

7. B. A. Kwetkus, Particle triboelectrification and its use in the electrostatic separation process. *Part. Sci. Technol.* **16**, 55-68 (1998).

8. C.-y. Liu, A. J. Bard, Electrostatic electrochemistry at insulators. *Nat. Mater.* **7**, 505-509 (2008).

9. C.-y. Liu, A. J. Bard, Chemical Redox Reactions Induced by Cryptoelectrons on a PMMA Surface. *J. Am. Chem. Soc.* **131**, 6397–6401 (2009).

10. A. F. Diaz, J. Guay, Contact charging of organic materials: ion vs. electron transfer. *IBM J. Res. Dev.* **37**, 249-259 (1993).

11. D. K. Davies, Charge generation on dielectric surfaces. *J. Phys. D: Appl. Phys.* **2**, 1533-1537 (1969).

12. C. B. Duke, T. J. Fabish, Contact electrification of polymers: A quantitative model. *J. Appl. Phys.* **49**, 315-321 (1978).

13. J. A. Wiles, B. A. Grzybowski, A. Winkleman, G. M. Whitesides, A tool for studying contact electrification in systems comprising metals and insulating polymers. *Anal. Chem.* **75**, 4859-4867 (2003).

14. L. S. McCarty, A. Winkleman, G. M. Whitesides, Ionic electrets: Electrostatic charging of surfaces by transferring mobile ions upon contact. *J. Am. Chem. Soc.* **129**, 4075-4088 (2007).

15. L. S. McCarty, G. M. Whitesides, Electrostatic charging due to separation of ions at interfaces: Contact electrification of ionic electrets. *Angew. Chem. Int. Ed.* **47**, 2188-2207 (2008).

16. R. Williams, The relation between contact charge transfer and chemical donor properties. *J. Colloid Interface Sci.* **88**, 530-535 (1982).

17. M. E. Labib, R. Williams, The use of zeta-potential measurements in organic solvents to determine the donor-acceptor properties of solid surfaces. *J. Colloid Interface Sci.* **97**, 356-366 (1984).

18. W. R. Harper, *Contact and Frictional Electrification* (Oxford University Press, London, 1967).

19. G. S. P. Castle, Contact charging between insulators. *J. Electrostat.* **40**, 13-20 (1997).

20. Z. Z. Yu, P. K. Watson, J. S. Facci, The contact charging of PTFE by mercury: the effect of a thiophene monolayer on charge exchange. *J. Phys D: Appl. Phys.* **23**, 1207-1211 (1990).

21. W. D. Greason, *21st Annual International Electrical Overstress/Electrostatic Discharge Symposium* (Elsevier Science B.V., Orlando, Florida, 1999), pp. 245.

22. R. Elsdon, F. R. G. Mitchell, Contact electrification of polymers. *J. Phys. D: Appl. Phys.* **9**, 1445-1460 (1976).

23. B. A. Grzybowski, M. Fialkowski, J. A. Wiles, Kinetics of contact electrification between metals and polymers. *J. Phys. Chem. B* **109**, 20511-20515 (2005).

24. B. A. Grzybowski, A. Winkleman, J. A. Wiles, Y. Brumer, G. M. Whitesides, Electrostatic self-assembly of macroscopic crystals using contact electrification. *Nat. Mater.* **2**, 241-245 (2003).

25. J. F. Kok, D. J. Lacks, Electrification of granular systems of identical insulators. *Phys. Rev. E* **79,** 051304, (2009).

26. J. Lowell, A. R. Akande, Contact electrification-why is it variable? *J. Phys. D: Appl. Phys.* **21,** 125-137 (1988).

27. V. Derjaguin, M. S. Metsik, Role of electrical forces in the process of splitting mica along cleavage planes. *Sov. Phys. Solid State (Engl. Transl.)* **1** , 1393-1399 (1960).

28. B. D. Terris, J. E. Stern, D. Rugar, H. J. Mamin, Contact electrification using force microscopy. *Phys. Rev. Lett.* **63,** 2669-2672 (1989).

29. V. Albrecht, A. Janke, E. Németh, S. Spange, G. Schubert, F. Simon, Some aspects of the polymers' electrostatic charging effects. *J. Electrostat.* **67**, 7-11(2009).

30. A. F. Diaz, R. M. Felix-Navarro, A semi-quantitative tribo-electric series for polymeric materials: the influence of chemical structure and properties. *J. Electrostat.* **62**, 277-290 (2004).

31. A. Luga, L. Calin, V. Neamtu, A. Mihalcioiu, L. Dascalescu, Tribocharging of plastics granulates in a fluidized bed device. *J. Electrostat.* **63**, 937-942 (2005).

32. M. M. Apodaca, P. J. Wesson, K. J. M. Bishop, M. A. Ratner, B. A. Grzybowski, Contact electrification between identical materials. *Angew. Chem.* **122**, 958-961 (2010); *Angew. Chem. Int. Ed.* **49**, 946-949 (2010).

33. Conformal, molecular-scale contact between PDMS and other materials provides the basis for the family of micro-contact printing techniques, whereby molecules (e.g., alkane thiols) are transferred from PDMS stamps onto various substrates (e.g., gold) to form self-assembled monolayers that are densely packed and uniform over large areas. In this and other applications, conformal contact is most readily achieved by curing PDMS prepolymer against atomically-flat silica wafers (as in our experiments). For details, see Y. N. Xia, G.M. Whitesides, *Annu. Rev. Mater. Sci.* **28**, 153-184 (1998) and Y. Xia, D.Qin, G. M. Whitesides, *Adv. Mater.* **8**, 1015-1017 (1996).

34. S. Kittaka, The generation of static charge on high polymer. *J. Phys. Soc. Japan*, **14**, 532-538 (1959).

35. G. M. Sessler, in *Electronic Properties of Polymers,* J. Mort, G. Pfister, Eds., (Wiley, New York, 1982), pp. 59-100.

36. B.B. Mandelbrot, *The Fractal Geometry of Nature* (Freeman, New York, 1983).

37. J. J. Cole, C. R. Barry, X. Wang, H. O. Jacobs, Nanocontact electrification through forced delamination of dielectric interfaces. *ACS Nano* **4**, 7492–7498 (2010).

38. G. Socrates, *Infrared and Raman Characteristic Group Frequencies* (Wiley, Chichester, UK, 2001)

39. Y. Israeli, J. Lacoste, J. Cavezzan, J. Lemaire, Photo-oxidation of olydimethylsiloxane oils Part II-effect of dimethylene groups. *Polym. Degrad. Stabil.* **42**, 267-279 (1993).

40. D. H. Chenery, Detection of peroxy species in ultra-high-molecular-weightolyethylene by Raman spectroscopy. *Biomaterials* **18**, 415-419 (1997).

41. W.R. Salaneck, A. Paton, Double mass transfer during polymer-polymer contacts. *J. Appl. Phys*. **47**, 144-147 (1976)

42. J. Lowell, The role of material transfer in contact electrification. *J. Phys. D: Appl. Phys*. **10**, L233-L235 (1977).

43. C. G. Camara, J. V. Escobar, J. R. Hird, S. J. Putterman, Correlation between nanosecond X-ray flashes and stick–slip friction in peeling tape. *Nature*, **455**, 1089-1093 (2008).
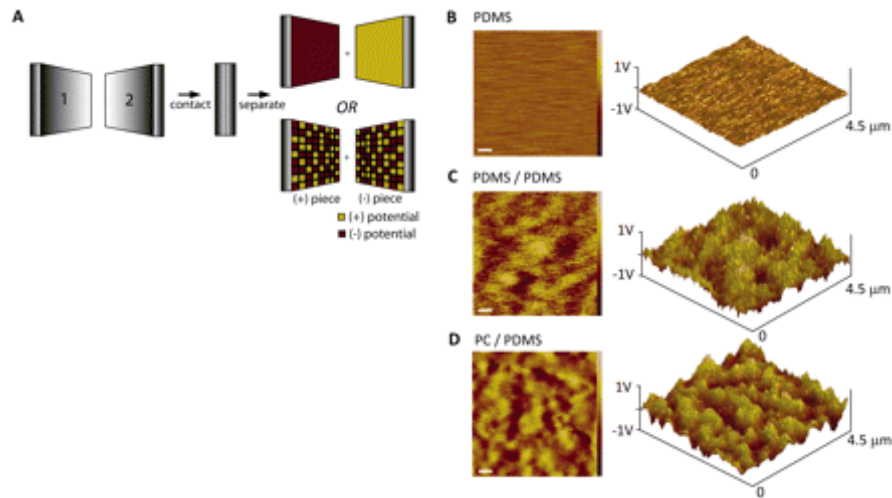
Fig. 1. Possible scenarios of contact electrification and experimental KFM surface potential maps. The traditional view in (**A,** *upper right*) assumes that upon contact and separation, one surface charges uniformly positively and the other, uniformly negatively. In contrast, the mosaic picture in (**A***, lower right*) assumes that each surface is a union of regions that have different propensities to accept or donate charge. Upon contact charging, these regions are then expected to develop different charge polarities. The mosaic picture of contact electrification is validated by the potential maps shown in (**B**)-(**D**). The map in (**B**) corresponds to PDMS before contact electrification. Such approximately uniform profiles were also observed for other "native" materials tested. In contrast, contact charged surfaces in (**C**) and (**D**) feature a "mosaic" of (+) and (-) regions. (**C**) PDMS charged negatively against another PDMS piece, (**D**) PC contact-charged positively against PDMS. The left column has 2D projections of the maps; on the right, the corresponding 3D maps are displayed. Color scale is adjusted to -1 V to 1 V in all images. Net surface charge densities on the contact-charged pieces (measured by Faraday cup prior to KFM measurements) were

A) 0.005, B) -0.20, and C) 0.16 nC/cm². All images have scan area of 4.5 ⌈m × 4.5 ⌈m; scale bars correspond to 500 nm.
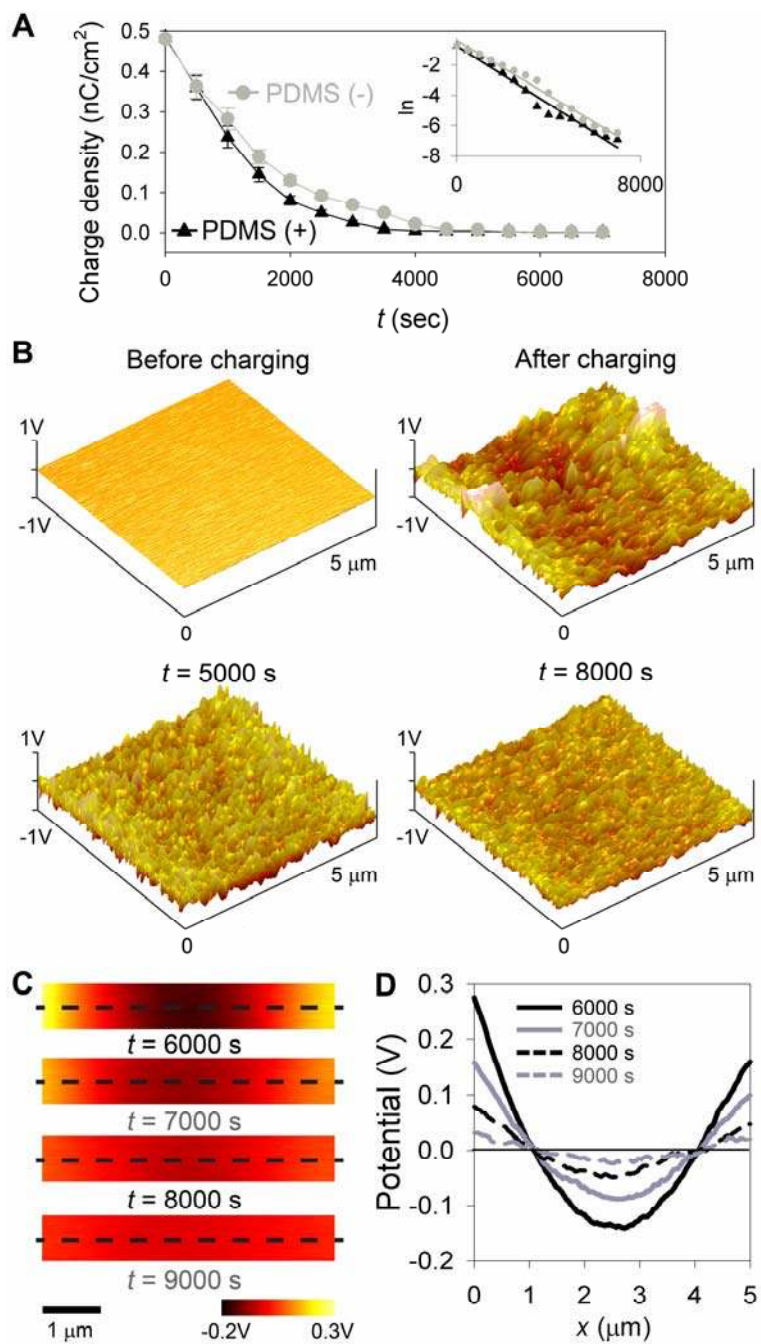
Figure 2. Kinetics of mosaic's discharge. **(A)** The magnitudes of the net charges (measured by a Faraday cup) on the negatively (gray circles) or the positively (black triangles) charged PDMS pieces decay with time. The decay rate constants, k_{dis}^{net}, are determined from the slopes of the semi-logarithmic plots in the inset and are $k_{dis}^{net} \sim 1 \times 10^{-3}$ s^{-1} for PDMS(+) and $k_{dis}^{net} \sim 0.9 \times 10^{-3}$ s^{-1} for PDMS (-). Similar magnitudes of the rate constants are observed for different types of contact-charged materials. **(B)** Typical KFM maps of a polymer (here, PDMS) before charging ($t = 0$ s), immediately after charging ($t = 3000$ s), and at two longer times $t = 5000$ and 8000 sec, when the charge within the mosaic dissipates. Discharge within the mosaics can be quantified from the line scans taken across the potential maps. In the example maps **(C)**, the dashed lines correspond to the line scans in **(D)**. Scale bar in **C** represents 1 μm. These potential profiles are related to surface charge densities and their evolution is modelled as first-order decay (see SOM, Section 2), with the decay rate constant $\sim 10^{-3}$ s^{-1}. Lateral migration of charge is found negligible (with effective diffusion constant $D < 1 \times 10^{-16}$ m^2/s)
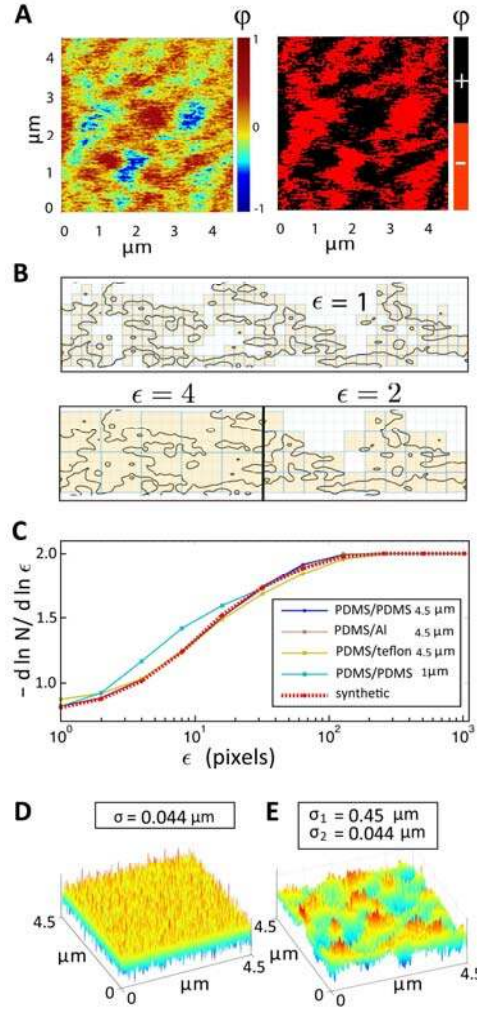
Fig. 3. Geometric universality of charge "mosaics". (A) A typical experimental KFM scan of electrostatic potential and the corresponding digitized map ("boundary set") delineating regions of positive and negative potentials. (B) Illustrates calculation of the local box counting (LBC) dimension of a potential map whereby the "wiggly" lines correspond to the boundaries between (+) and (-) regions. The map is covered by grids of different box sizes (here, □ = 1,2,4). Next, for a given □ , the number of boxes, N(□), through which the wiggly lines/boundaries are passing is calculated – in the figure, these boxes are shaded in

light pink. Finally, LBC dimension is calculated as $L_{BC}(\varepsilon) = -\dfrac{d \ln N(\varepsilon)}{d \ln \varepsilon}$. Plotting it for

different values of □ (in experimental KFM maps ε = 1 pixel to ε = 1024 pixels, scan area 4.5 □m × 4.5 □m) yields profiles such as those in (C). (C) LBC profiles for boundary sets from different KFM scans and a modeled profile corresponding to a two-scale random field

17

($\square_1$=0.45 $\square$m and $\square_2$=0.044 $\square$m; dotted red line). (D) Image of a random field with a single scale of fluctuations, $\square$ and (E) of a field with two spatial fluctuation scales $\square_1$=0.45 $\square$m and $\square_2$ =0.044 $\square$m corresponding to the modeled LBC profile in (C)).
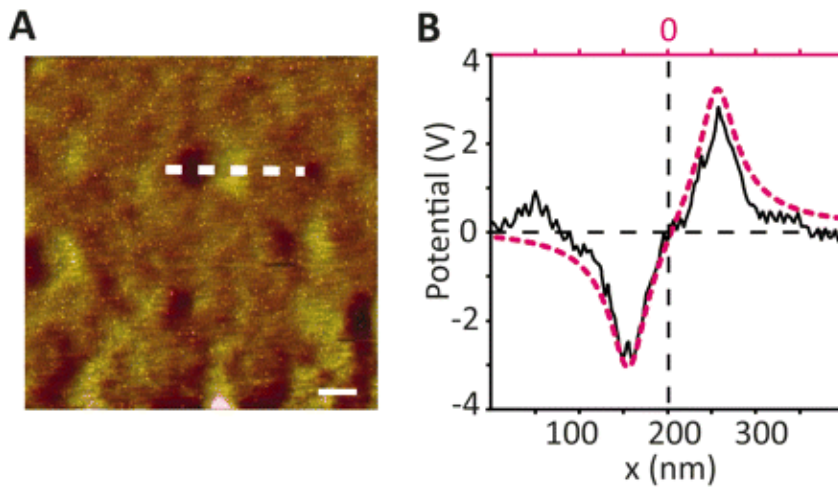
Fig 4. **Deducing charge density within the mosaic's islands from high-resolution KFM scans of an electrified surface.** (**A**) A typical KFM potential map (here, PDMS charged against PDMS); white line corresponds to the line over which the potential profile in (**B**) was taken (black line). Red, dotted curve in (B) gives a potential profile calculated above (at ∼ 100 nm, corresponding to the elevation of the KFM tip) a plane presenting two oppositely charged, nearby "islands". Theoretical potential fits the experimental profile assuming that each of the nanoscopic islands comprises ca. 500 elementary charges (corresponding to surface charge ∼ $\lceil$C/cm^2). Scale bar in (A) corresponds to 100 nm.
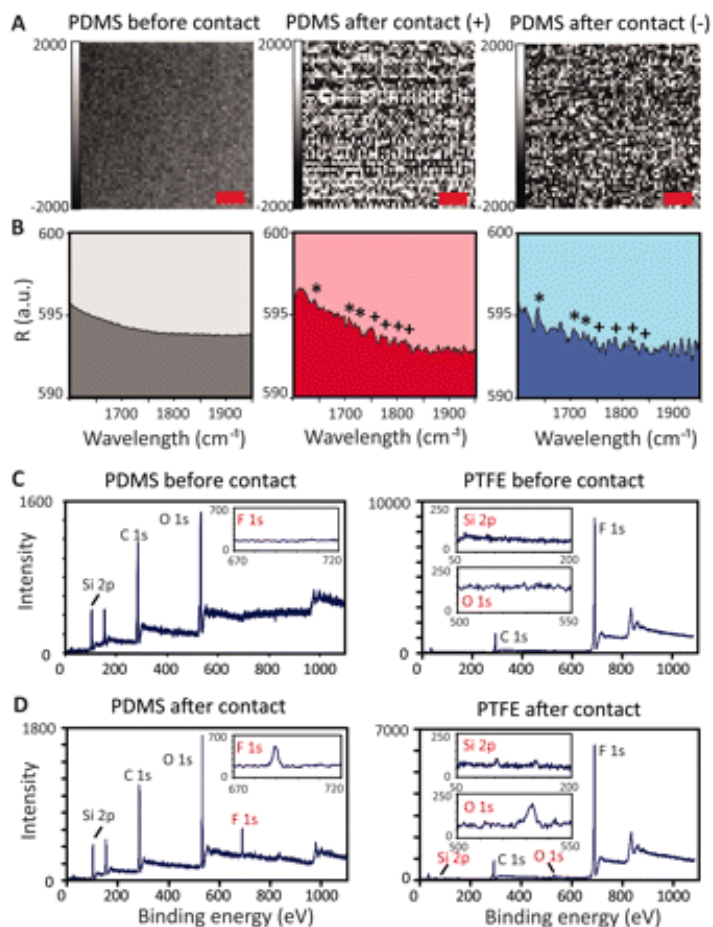
Fig. 5. The microscopic basis of charged mosaics. (**A**) Confocal Raman microscopy images of (*left*) an uncharged PDMS piece (using a gold coated silicon wafer as background); (*middle*) positively charged and (*right*) negatively charged PDMS pieces contact-charged against one another (in both cases, uncharged PDMS piece was taken as a background). Scale bars =2 ⌈m. (**B**) Total Raman spectra (*R*= Raman Intensity) of the regions mapped in (A). The peaks at 1642 cm^{-1} and 1710-1730 cm^{-1} for SiCH$_2$COOH (marked with "**∗**"), and between 1730-1830 cm^{-1} for SiCOOH and RCOOOH where R=Si or C (marked with "**+**") (*38-40*) increase in comparison to the non-contacted piece thus

indicating chemical modifications occurring upon contact charging. These modifications are accompanied by material transfer, as evidenced by the XPS spectra of a PTFE/PDMS pair in **(C)** and **(D)**. Insets showing the high resolution spectra demonstrate transfer of PTFE onto PDMS (appearance of F 1s peak at 690 eV) and of PDMS onto PTFE. (appearance of Si 2p at 102.5 eV and O 1s at 533 eV peaks).

Supporting Online Material for Manuscript entitled "*The mosaic of surface charge in contact electrification*" by H. T. Baytekin, A. I. Patashinski, M. Branicki, B. Baytekin, S. Soh, B. A. Grzybowski*

CONTENTS:

Section 1. Further experimental details.

Section 2. Modeling the discharging of the mosaics.

Section 3. LBC profiles of experimental and simulated surface charge distributions.

Section 4. Additional Raman spectra at different depths.

Section 5. Additional XPS spectra demonstrating material transfer.

****

Section 1. Further experimental details. The materials used in most of our experiments were aluminum foil (purchased from VWR international), polytetrafluoroethylene (PTFE, from McMaster-Carr, CAT# 8545K26), polycarbonate (PC, from McMaster-Carr, CAT# 8574K172) and poly(dimethylsiloxane) (PDMS). PDMS was prepared by mixing a degassed elastomer base and a crosslinker in a 10:1 w/w ratio (Sylgard 184, Dow Corning). Prepolymer mixture was cast on an atomically flat [100] silicon wafer (Montco Silicon Technologies, Inc.), silanized with 1H, 1H, 2H, 2H-perfluorooctyltrichlorosilane and was cured at 65 $^{\circ}$C for 24 h. After curing the prepolymer, the PDMS pieces (ca. 1cm × 1cm × 0.4cm) were gently peeled off the wafer.

Prior to contact-charging, pieces of all materials were left to discharge for at least 24 hrs under argon. The electroneutrality (i.e., lack of any detectable net charge) of all materials was confirmed by (1) measurements using a house-made Faraday cup connected to a high precision electrometer (Keithley Instruments, model 6517B). Only pieces with charge densities below the electrometer's detection limit $<\pm0.005$ nC/cm^2, were considered to be neutral (vs. densities above 0.1-0.2 nC/cm^2 after charging) and used in further experiments; (2) KFM potential imaging; here neutrality was assumed if the highest potential on the scanned surface did not exceed 10 mV (vs. > 500 mV for electrified pieces).

All experiments were performed under ambient conditions (typically, temperature ~22 ^{o}C, relative humidity ~24 %). The Faraday cup was also used to measure net charges on the contact-electrified materials.

KFM measurements were performed on a Veeco Dimension Icon Scanning Probe Microscope. Pt/Ir coated tips (SCM-PIT) were purchased from Veeco Probes (tip radius curvature $\leq$ 20 nm, spring constant 2.8 N/m, and resonant frequency of 75 kHz). Raman confocal microscopy was performed on Nanophoton Raman 11 microscope with pixel resolution of 250 nm × 250 nm. X-ray photoelectron spectroscopy (XPS) analyses were performed with an Omicron ESCA probe, which was equipped with EA125 energy analyzer. Photoemission was stimulated by a monochromatic Al K alpha radiation (1486.6 eV) with the operating power of 300 W. Survey scan and high-resolution scan were collected using pass energies of 70 and 26 eV, respectively. Analyzer substrate angel was

45$^{\text{o}}$. Binding energies of spectra were referenced to the C 1s binding energy set at 285 eV. At least 3 different measurements were performed for each sample.

**Section 2. Modeling the discharging of the mosaics.**

Gradual decay of charge from the mosaic's patches can be modeled based on the potential profiles such as those shown in Figures 2C and 2D in the main text. In general, charge dissipation can be due to the so-called "external decay" via collisions with molecules in the surrounding atmosphere, or due to the "lateral" charge migration in the plane of the support (with concomitant "neutralization" of charges of opposite polarities) (*35*). Noting that the potentials recorded by the KFM instrument are proportional to the surface charge densities, *q* (J.W. Hong, S.-i. Park, Z.G. Kim, *Rev. Sci. Instr.* 70, 1735-1739, 1999), a simple model accounting for both modes of charge decay can be written in terms of reaction-diffusion equations:

$$\frac{\partial q^+}{\partial t} = D^+ \frac{\partial^2 q^+}{\partial x^2} - k_d^+ q^+ - k_n q^+ q^-$$

$$\frac{\partial q^-}{\partial t} = D^- \frac{\partial^2 q^-}{\partial x^2} - k_d^- q^- - k_n q^+ q^-$$

In these equations, positive and negative charge densities are denoted by q^+ and q^-, respectively, D^+ and D^- stand for the effective diffusion coefficients of charges (charge transport in dielectrics has been demonstrated as diffusive in previous works (D. Mandler, P.R. Unwin, *J. Phys. Chem. B.,* **107**, 407-410, 2003; Y. Hori, *Journal of Electrostatics*, **48**, 127-143, 2000), k_d's are the rates of external discharge, k_n represents the rate of (rapid) charge neutralization when the charges of the opposite polarities are found at the same

location, and $x = [0,L]$ is the domain of the problem corresponding to the directions along which the scans in Figs. 2C,D are taken. For different values of the parameters listed above and for appropriate initial and boundary conditions (e.g., symmetric boundary conditions at the ends of the domain; $\partial q^+ / \partial x\big|_{x=0,L} = 0$ and $\partial q^- / \partial x\big|_{x=0,L} = 0$, where $L = 2$ μm), these equations can be integrated numerically (here, using finite element method implemented with Comsol Multiphysics software).

First, we consider the case when charge mobility is appreciable. A typical situation is then illustrated in Fig. S1A and S1B, which shows the evolution of a charge profile between two nearby, oppositely charged patches. Initially, in Fig. S1A, the left patch is charged positively (red), and the right patch is charged negatively (blue). After integrating the RD equations for times commensurate with the experimental conditions (thousands of seconds, cf. Fig. 2C in the main text), the profiles change. If the diffusion coefficient is appreciable (D^+ and/or $D^- > \sim 10^{-16}$ m^2/s), the profiles not only decay in magnitude but also characteristically "broaden" while the position of the "zero"– indicated by the arrows in Fig. S1 – changes. This situation corresponds to the charged patches becoming blurry as they discharge. In sharp contrast, when the values of D's are smaller (Fig. S1C), the profiles broaden much less and the position of the "zero" is virtually unchanged. Comparing with the experimental profiles in Fig. 2D where the positions of the "zero" are not changing with time, we conclude that in our experiments, lateral charge mobility is negligible.
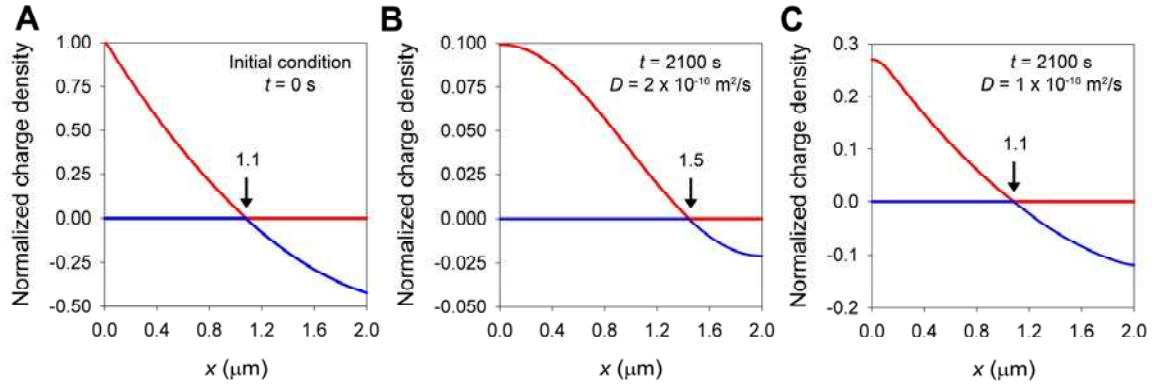
Figure S1. Evolution of charge profiles starts from the initial conditions in **(A)**. In **(B)**, the charge mobility is relatively large (here, $D = 2\times 10^{-16}$ m^2/s), the profile decays and broadens with time, and its "zero" moves to ~1.5 μm. In **(C)**, charge mobility is significantly lower ($D = 1\times 10^{-18}$ m^2/s), broadening is much less pronounced, and the position of the "zero" hardly changes. In both cases, the integration times were 2100 sec and the particular kinetic rates were taken as $k_d^+ = k_d^- = 6\times10^{-4}\,\text{s}^{-1}$ and $k_n = 1 \times 10^4$ m^2/C·s. The general conclusions, however, do not depend on these kinetic parameters which control the "vertical" decay of charge, not lateral mobility.

Given the negligible role of lateral charge mobility, the RD equations can be simplified to simple O.D.E.s $\dfrac{dq^+}{dt} = -k_d^+ q^+$ and $\dfrac{dq^-}{dt} = -k_d^- q^-$ which, in conjunction with data such as that in Fig. 2D, can be used to fit kinetic rate constants describing discharging of the (+) and (-) patches. This procedures yield the values of $k_d^+ \sim k_d^- \sim 10^{-3}$ s^{-1}, which agree with the "macroscopic" decay rate constants (cf. Fig. 2A).

Section 3. LBC profiles of experimental and simulated surface charge distributions.

The LBC profiles of the boundaries separating the (+) and (-) regions in the surface potential KFM scans are shown in Fig. 3C in the main text. In this Section, we compare these results with LBC profiles obtained for various types of computer-generated potentials which contain random fluctuations introduced at a hierarchy of spatial scales (technically speaking, these synthetic potentials are realized by the so-called "smooth random scalar fields").

Given the scan area D, the random fields used for constructing the synthetic potential are generated by first choosing a family of square meshes covering D and having different periodicities/mesh sizes σ_k, where k belongs to an ordered set of real numbers such that σ_1 is the coarsest mesh and σ_k is the finest mesh. Then, for each mesh in this family, every grid point is assigned a z-component of magnitude drawn randomly from a Gaussian distribution with zero mean and variance one. The random z-components assigned to the points of each mesh are chosen independently and are statistically uncorrelated. Consequently, the distance between the neighboring points in each mesh can be associated with a scale of fluctuations. If only a single fluctuation scale is present, it can be thought of as the characteristic island size. The synthetic potential with a number of different fluctuation scales is generated by a superposition of random fields constructed for each mesh in the family.

The LBC profiles (cf. caption to Fig. 3B in the main text) computed for such random fields with a single fluctuation scale do not agree with those obtained for the experimental scans. In the examples shown in Fig. S2A-C, the synthetic potentials were obtained by generating random fluctuations at points of a single mesh with periodicity σ_k for $k = 2, 3,$

5, and *20* pixels*;* the mesh used for analysis contains 1024 × 1024 pixels. Varying the fluctuation scale (i.e., the mesh size σ_k) results in an overall shift of the synthetic LBC profiles but it has little effect on their slope, which remains steeper than for the LBC profiles measured for the experimental potentials. The observed shift of the LBC profiles merely indicates that for a decreasing scale of fluctuations in the examined potentials, a smaller box size has to be used in the LBC measure in order to detect the structural details of the boundary set.

In contrast, we find that experimental LBC profiles agree with synthetic profiles incorporating two different length scales σ_1 and σ_2. The structure of the mosaics recorded by KFM is best reproduced (in the LBC sense) for synthetic fields with $\sigma_1 = 110$ pixels (0.45 ⌈m) and $\sigma_2 = 10$ pixels (0.044 ⌈m), as illustrated in Fig. S2D-F.
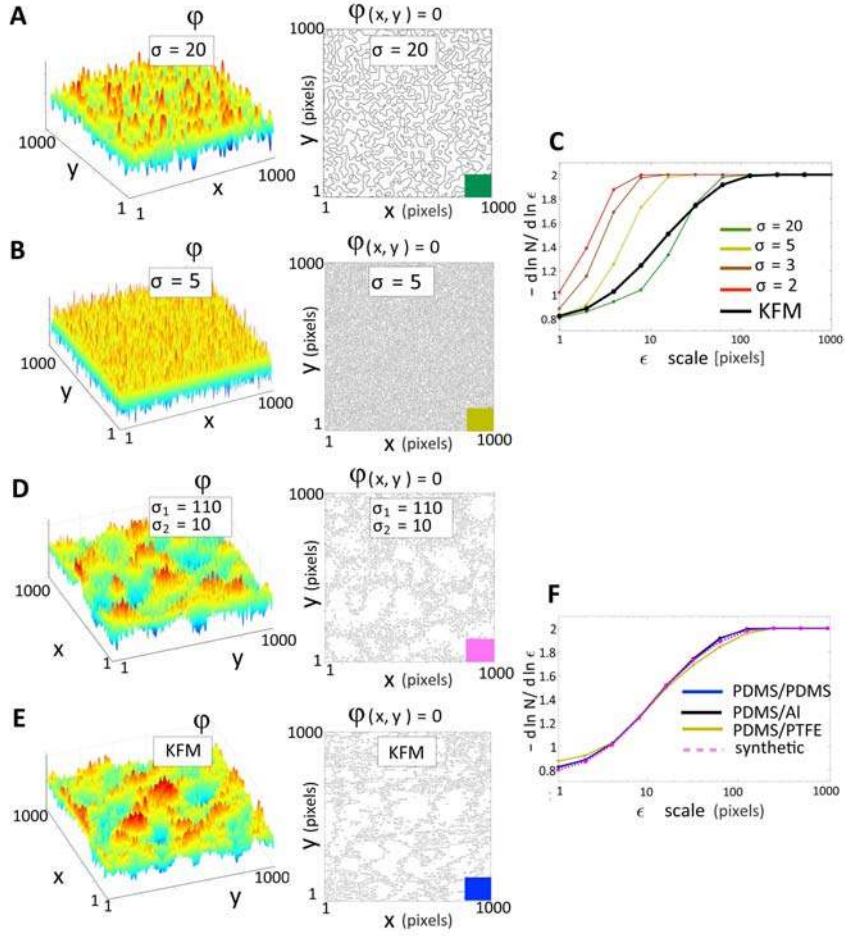
Fig. S2. (**A-B**) Examples of simulated random fields with single fluctuation scale ∫, their zero level sets (i.e., boundaries between the "+" and "-" regions) and (**C**) corresponding profiles of L_{BC}. Single-scale random fields cannot reproduce the experimental potential structure (black curve), (**D-F**) Comparison between LBC profile obtained from a random field with two spatial fluctuation scales and the experimental KFM scans. The experimental LBC profiles are the same as in Fig. 3 in the main text and the best agreement is obtained from a simulated random field with ∫$_I$=110 pixels (about 0.45 ∫m) and ∫$_I$=10 pixels (about 0.044 ∫m).

Section 4. Additional Raman spectra at different depths.
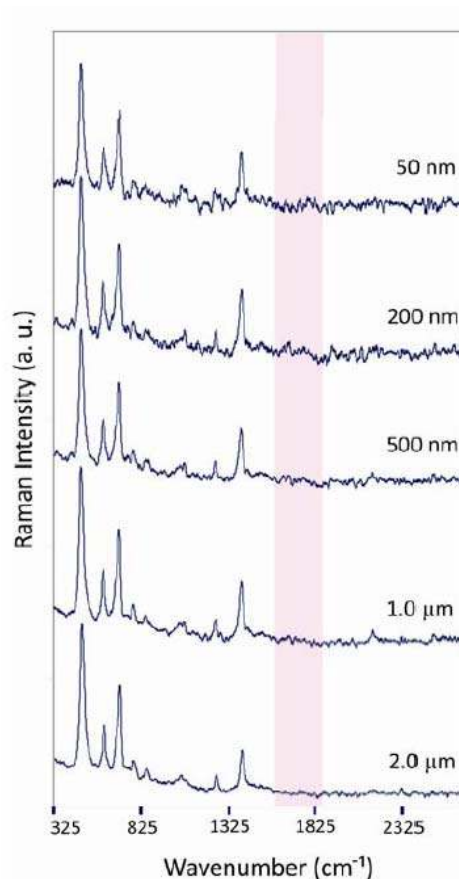
Fig S3. Total Raman spectra of a negatively charged PDMS piece contact-charged against another PDMS piece. The region shaded in pink contains peaks at 1642 cm^{-1} and 1710-1730 cm^{1} (SiCH$_2$COOH) and between 1730-1830 cm^{-1} (RCOOH and RCOOOH, where R=Si or C) characteristic of compositional changes due to contact electrification. The intensity of these peaks decreases as the scan depth is increased from 50 nm to 2.0 ⌈m, confirming that contact-electrification affects predominantly the layer of the material near the surface – this observation agrees with multiple other studies on contact-electrification (*16-19*).

Section 5. Additional XPS spectra demonstrating material transfer.
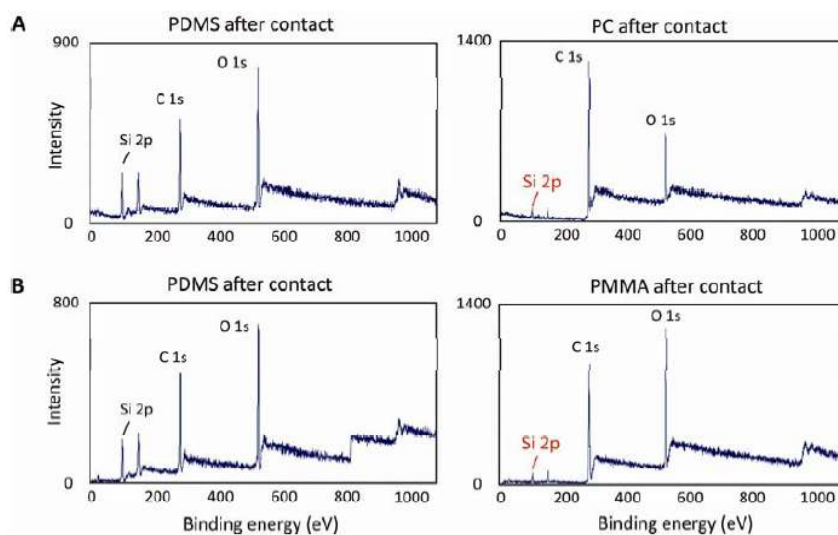
Fig. S4. XPS spectra of (**A**) PDMS/PC and (**B**) PDMS/PMMA after contact electrification. Transferred of PDMS onto PC and PMMA is evidenced by the appearance of a characteristic Si 2p peak at at 102.5 eV.